

Titel/Title:

Autor*innen/Author(s):

Veröffentlichungsversion/Published version:

Publikationsform/Type of publication:

Empfohlene Zitierung/Recommended citation:

Verfügbar unter/Available at:

(wenn vorhanden, bitte den DOI angeben/please provide the DOI if available)

Zusätzliche Informationen/Additional information:

1 Incision of submarine channels over pockmark trains in the South China Sea

2
3 **Kaiqi Yu^{1,2,3}, Elda Miramontes^{4,5}, Tiago M. Alves⁶, Wei Li^{1,2,3*}, Linlin Liang^{3,7}, Shuang Li^{1,}**
4 **^{2,3}, Wenhuan Zhan^{1,2,3}, and Shiguo Wu^{3,8}**

5 ¹Key Laboratory of Ocean and Marginal Sea Geology, South China Sea Institute of Oceanology,
6 Innovation Academy of South China Sea Ecology and Environmental Engineering, Chinese Academy
7 of Sciences, Guangzhou 510301, China.

8 ²Southern Marine Science and Engineering Guangdong Laboratory (Guangzhou), Guangzhou
9 511458, China.

10 ³University of Chinese Academy of Sciences, Beijing 100049, China.

11 ⁴Faculty of Geosciences, University of Bremen, Bremen 28359, Germany.

12 ⁵MARUM-Center for Marine Environmental Sciences, University of Bremen, Bremen, 28359,
13 Germany.

14 ⁶3D Seismic Laboratory, School of Earth and Environmental Sciences, Cardiff University, Main
15 Building, Park Place, Cardiff, CF10 3AT, United Kingdom.

16 ⁷State Key Laboratory of Tropical Oceanography, South China Sea Institute of Oceanology, Chinese
17 Academy of Sciences, Guangzhou, China.

18 ⁸Institute of Deep-sea Science and Engineering, Chinese Academy of Sciences, Sanya, 572000,
19 China.

20 *Corresponding authors: Dr. Wei Li (wli@scsio.ac.cn)

21 **Key Points:**

- 22 • A complex system of channels in the western South China Sea was formed by the erosion of
23 seafloor pockmarks.
- 24 • The evolution from pockmarks to channel comprises three stages: pockmark train, immature,
25 and mature channel.
- 26 • This on-going system of channels was initiated in the Late Miocene and was significantly
27 influenced by seafloor topography.
28

29 **Abstract**

30 The genesis of submarine channels is often controlled by gravity flows, but channels can also be
31 formed by oceanographic processes. Using multibeam bathymetry and two-dimensional seismic data
32 from the western South China Sea, this study reveals how pockmarks ultimately form channels under
33 the effect of bottom currents and gravity-driven sedimentary processes. We demonstrate that
34 alongslope and across-slope channels were initiated by pockmark trains on the seafloor. Discrete
35 pockmarks were elongated due to the erosion of gravity-driven sedimentary processes and bottom
36 currents, and later coalesced to form immature channels with irregular thalwegs. These gradually
37 evolved into mature channels with continuous overbanks and smooth thalwegs. Submarine channel
38 evolution was significantly influenced by seafloor topography since the Late Miocene. The
39 evolutionary model documented here is key to understanding how channels are formed in deep-water
40 environments.

41 **Plain Language Summary**

42 Submarine channels are prominent erosional features on continental slopes and basin floors. They are
43 usually formed by ocean currents flowing alongslope and sediment avalanches flowing downslope.
44 Here, we investigate a system of channels on the western South China Sea using geophysical methods.
45 The channels are formed in a region with widespread seafloor depressions (pockmarks) formed by
46 the seepage of fluid into the water column. Gravity-driven sedimentary processes and ocean currents
47 reshaped these pockmarks, which were ultimately merged together to form immature and irregular
48 channels. Under continued erosion, the immature channels eventually developed mature channels
49 with continuous overbanks and smooth channel floors. This study reveals that ocean currents and
50 gravity processes can form channels with different orientations by eroding pre-existing pockmarks.

51

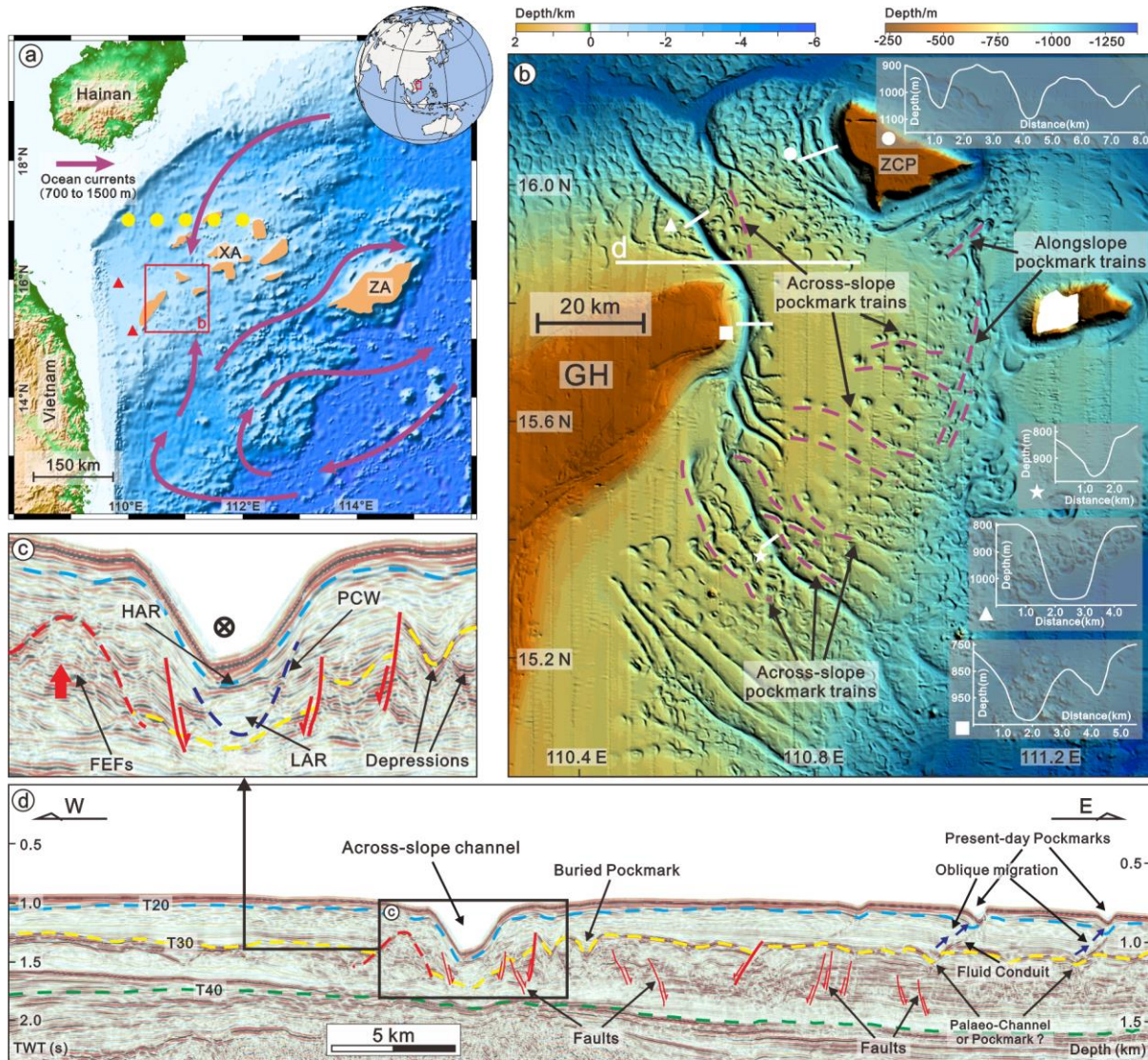
52 **1. Introduction**

53 Submarine channels are erosional features that can be several km-wide and 10s to 100s km-long
54 and are commonly found on continental margins and abyssal plains (Fildani et al., 2013; Hansen et
55 al., 2017; Lemay et al., 2020). They are important elements of source-to-sink depositional systems,
56 and can gather abundant paleoceanographic and paleoclimatic information in their constituent
57 channel-fill deposits (Hernández-Molina et al., 2003; Zhu et al., 2010; Allen, 2017). The generation
58 of channels transverse to continental slopes is mainly controlled by gravitational processes (Fildani
59 et al., 2013; Li et al., 2015; de Leeuw et al., 2016), but can also be influenced by oceanographic
60 processes such as dense shelf-water cascading and internal waves (Puig et al., 2014). In contrast,
61 contour currents are the primary control on the evolution of channels parallel to the slope bathymetry
62 (Rebesco et al., 2014; García et al., 2009; Stow et al., 2013; Miramontes et al., 2020; 2021).

63 Large numbers of crater-like depressions co-exist with channels in regions such as the Gulf of
64 Cadiz (León et al., 2010), West Africa (Pilcher and Argent, 2007), Mediterranean Sea (Miramontes
65 et al., 2019), and New Zealand (Hillman et al., 2018). These crater-like depressions comprise seafloor
66 pockmarks generated by the erosional power of focused fluid vents on soft sediment (Hovland et al.,
67 2002; Dandapath et al., 2010). Their size and shape depend on the activity of the fluid seeping through
68 them, the grain size of near-seafloor sediment, and the erosional power of currents (Gay et al., 2007).
69 Importantly, seafloor pockmarks can also be reshaped by downslope and alongslope processes to
70 form pockmark-related morphologies such as gullies, furrows and comet structures (León et al., 2010;
71 Kilhams et al., 2011).

72 Despite the above, it is still unclear whether pockmarks can evolve into channels, and which
73 processes control their morphology. In order to decipher the latter processes, this study aims to: (1)

74 characterize the morphology and internal architecture of channels in a poorly studied part of the South
75 China Sea; (2) reconstruct the initiation and interpret the processes controlling the development of
76 the investigated channels; and (3) reveal the role of pockmarks in submarine channel incision. The
77 Western South China Sea is an ideal region to study the evolution of pockmarks because their origin
78 is well known (Lu et al., 2017), and submarine channels with different orientations and sizes are
79 abundant (Figure 1).



80

81 **Figure 1.** Location, oceanography and seismic-stratigraphic markers of the study area. a) Bathymetric
82 map of the western South China Sea revealing the location of the study area. The purple arrows
83 indicate the circulation direction at a water depth of 700-1500 m based on Quan and Xue (2018). The
84 yellow dots indicate the location of the speed profiles for the ocean currents shown in Figure S9 of
85 the supporting information that were acquired with a vessel-mounted ADCP (2009-2012) and
86 published by Yang et al. (2019). The red triangles show the location of sediment cores collected for
87 grain size analysis of sea-bottom sediments (Astakhov, 2004a; b). XA and ZA indicate the location
88 of the Xisha and Zhongsha Archipelagos, respectively. b) Multibeam bathymetric map showing the
89 submarine channels and pockmarks studied in this study. The bathymetric profiles show the geometry
90 of channel cross-sections. The purple dashed lines indicate the tracks of across-slope and alongslope
91 pockmark trains. GH: Guangle High; ZCP: Zhongjianbei Carbonate Platform. c) A zoomed-in inset
92 of the seismic profile shown in (d) highlighting the internal architecture of an across-slope channel.

93 The dashed dark-blue line reveals the base and wall of the oldest paleo-channel observed under a
94 modern submarine channel. d) Two-dimensional seismic profile showing regional stratigraphic units
95 (based on Lu et al., 2017) and main structures around the studied channel system. The dark blue
96 arrows indicate the oblique migration of pockmarks towards the east. Seismic horizons T20, T30 and
97 T40 correlate with the bases of Quaternary, Pliocene and Late Miocene strata, respectively.
98

99 2. Materials and Methods

100 High-resolution multibeam bathymetric data and two-dimensional (2D) multi-channel seismic
101 reflection profiles are used in this study.

102 The multibeam bathymetric data were acquired in 2008 by the Guangzhou Marine Geological
103 Survey (GMGS) using a SeaBeam 2112 system. The dataset covers an area of $\sim 10,000$ km² with a
104 water depth range between 300 m and 1300 m. These bathymetric data have a horizontal resolution
105 of ~ 100 m (cell size) and a vertical resolution of ~ 3 m (3‰ of the water depth). The data were
106 imported and analyzed in Global Mapper[®].

107 Two-dimensional (2D) seismic reflection data were acquired by the China National Petroleum
108 Company (CNPC) in 2005 and processed by the PetroChina Hangzhou Research Institute of Geology.
109 The data were migrated with a common midpoint (CMP) spacing of 12.5 m and a main frequency
110 bandwidth of 30 Hz to 45 Hz (main frequency: 35 Hz). The vertical resolution of the seismic data
111 approaches 25 m. The 2D seismic data were interpreted on Landmark[®]. The ages of main seismic
112 stratigraphic markers were based on Lu et al. (2017).

113 In order to provide a reference about the typical values of current velocity in the western South
114 China Sea, we show in Figure S9 of the supporting information the average currents along a transect
115 (see location in Fig. 1a) during four different years (2009, 2010, 2011 and 2012). Current
116 measurements were acquired using a vessel-mounted ADCP Ocean Surveyor 38kHz (OS38) and were
117 published by Yang et al. (2019).

118

119 3. Regional setting

120 3.1. Geological setting

121 The South China Sea was formed from Oligocene to the middle Miocene and is the largest (~ 3.5
122 $\times 10^6$ km²) and deepest (> 5000 m) marginal sea in the western Pacific Ocean (Zhou et al., 1995; Li
123 et al., 2014). The study area lies southwest of the Xisha Archipelago on a topographic high identified
124 between two drowned carbonate platforms, the Guangle High (GH) and the Zhongjianbei Carbonate
125 Platform (ZCP) (Figure 1b). Pockmarks are abundant and relate to regional hydrothermal activity and
126 gas seepage (Lu et al., 2017; Gao et al., 2019). Sediment cores collected to the west of the study area
127 (Figure 1a) indicate that bottom sediment is composed of silt, with the particle diameter representing
128 the 50% cumulative percentile value (D50) ranging between 5 and 50 μm (Astakhov, 2004a; b; Figure
129 1a).

130 This study focuses on the shallow strata of the western South China Sea, which can be
131 subdivided into three seismic-stratigraphic units: Unit 1 (Quaternary); Unit 2 (Pliocene) and Unit 3
132 (Late Miocene). The bases of these units correlate with seismic horizons of T20, T30 and T40,
133 respectively (Figures 1d and S1). The seismic-stratigraphy of the study area is interpreted based on
134 regional correlations with adjacent regions (Lu et al., 2017).

135 3.2. Oceanographic setting

136 The South China Sea is a semi-enclosed marginal sea connected to the Pacific Ocean through
137 the Luzon Strait (Liu et al., 2008). At present, the western South China Sea comprises four main water
138 masses: surface water (at a water depth between 0 and 750 m), intermediate water (at water depths
139 between 750 and 1500 m), deep and bottom waters deeper than 1500 m (Quan and Xue, 2018; Yin et
140 al., 2021). Quan and Xue (2018) proposed a layered circulation model for the western South China
141 Sea, in which current direction between 700 and 1500 m water depth is to the south in the northern
142 part of the study area, but changing to a northward direction in the southern part (Figure 1a).
143 According to the vessel-mounted ADCP data from Yang et al. (2019), ocean currents close to the
144 study area show a variable behavior, with their average speed ranging from 10 to 20 cm/s. The
145 measured maximum speed of ocean currents reaches 80 cm/s (Figures 1a and S9).

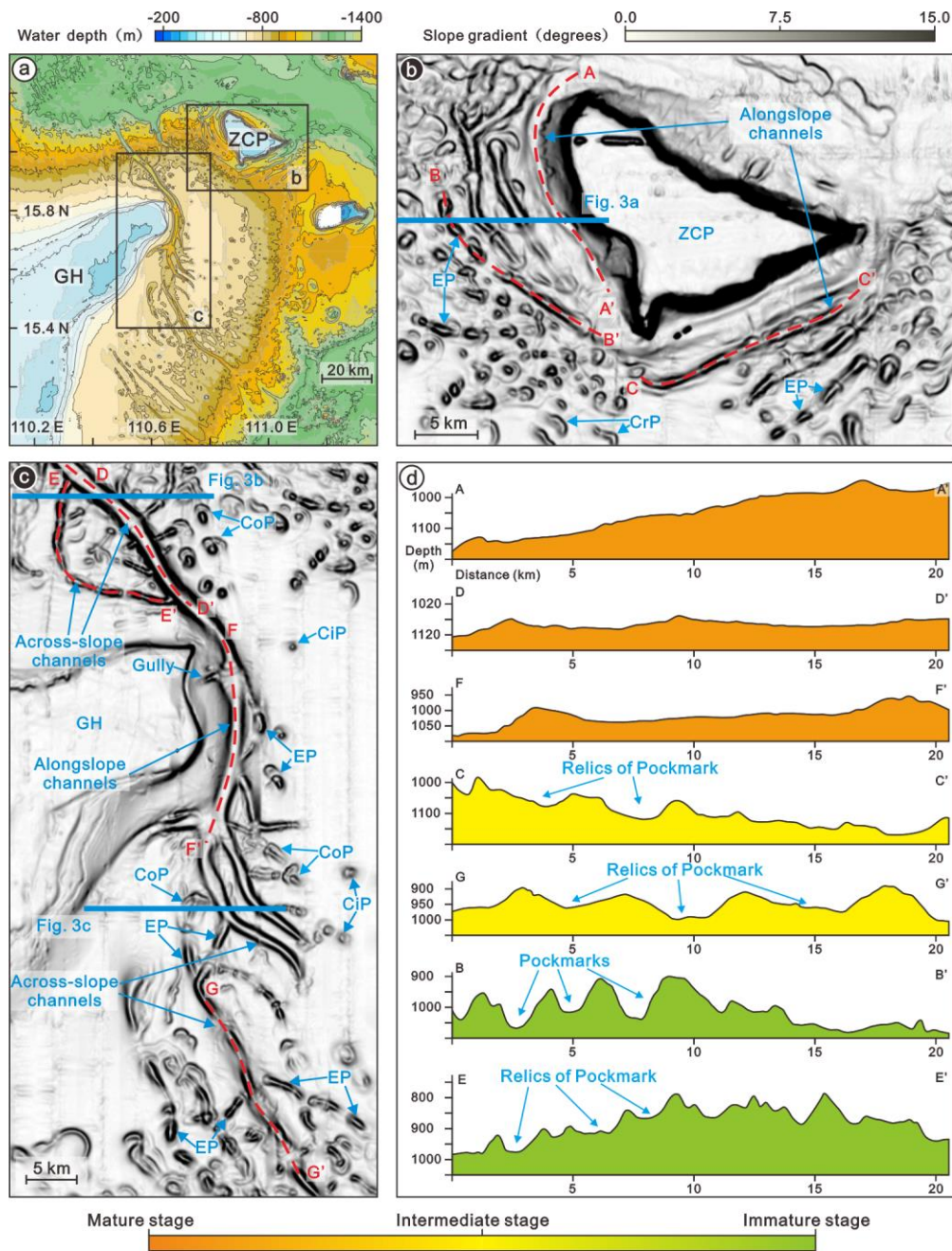
146

147 **4. Giant pockmark field**

148 A giant pockmark field covering an area of more than 9,000 km² is recognized on the multibeam
149 bathymetric map in Figure 1b. Pockmarks are widespread and generally arranged in continuous trains
150 of pockmarks (Figure 1b). These pockmark trains are divided into two main categories: alongslope
151 and across-slope. Pockmark trains that are parallel to the regional bathymetric contours, or located
152 around bathymetric highs, are herein named “alongslope pockmark trains”. This category includes
153 pockmarks formed around the ZCP and in the eastern part of study area (Figures 1b and 2b). The
154 second category is named “across-slope pockmark trains” and comprises those aligned in a trend
155 perpendicular to the bathymetric contours (Figure 1b). Across-slope pockmark trains are observed in
156 the slopes south, east and north of the GH, at a water depth ranging from 750 to 900 m (Figures 1b
157 and 2a).

158 Bathymetric data reveal that pockmarks are diverse in their geometry and dimensions (Figures
159 2 and S8). Pockmark depth oscillates between 50 and 180 m, with a maximum diameter from 1 to 3
160 km (Figure S8). Pockmarks are also variable in plan-view comprising elongated, comet-shaped,
161 circular and crescent-shaped features (Figures 1b, 2b and 2c). Circular pockmarks are relatively small
162 and often isolated when compared to the three other types, with pockmark widths between 0.8 and
163 1.5 km (Figures 2c and S8). Crescent pockmarks are shaped as slender curves and distributed in
164 groups; their concave side is aligned in the same direction (Figure 2b). Comet-shaped and elongated
165 pockmarks are 1-3 km wide and 80-170 m deep, values that are similar to the width and depth of
166 adjacent channels. They are usually aligned and show a consistent orientation (Figures 2b and 2c).

167 Seismic profiles reveal that most pockmarks are formed during or after the Pliocene, as they
168 occur above or truncate horizon T30 (Figures 1d and 3), with only a few forming before the Pliocene
169 (Figure S6). This is a character further discussed in Section 6 of this paper.



170

171 **Figure 2.** a) Bathymetric contour map revealing the distribution of submarine channels between the
 172 Guangle High (GH) and the Zhongjianbei Carbonate Platform (ZCP). b) and c) Slope gradient maps
 173 showing the morphology of channels and pockmarks around the GH and ZCP. Red dashed lines
 174 indicate the thalwegs of the channels depicted in the topographic profiles in (d). Solid blue lines
 175 indicate the location of the seismic profiles in Figure 3. CiP-Circular Pockmark; CoP-Comet
 176 Pockmark; CrP-Crescent Pockmark; EP-Elongated Pockmark. d) Topographic profiles highlighting
 177 the axial morphology of channels and semi-connected pockmarks near the heads of discrete channels
 178 (e.g. B-B'). Green, yellow and orange colors indicate the channels that are immature, intermediate
 179 and mature in their evolution. Detailed morphometric data for the submarine channels is given in
 180 Table S1.

181

182 5. Channel systems

183 The studied submarine channels can be classified into alongslope and across-slope channels
184 based on their orientation and geometry (Figures 1b and 2). In addition, they have been defined as
185 mature and immature channels based on: a) the roughness of their thalwegs, and b) the relative
186 continuity of channel plane morphology (Figure 2, Table S1). In essence, mature channels reveal
187 smoother thalwegs and a more continuous morphology when compared to immature channels (Figure
188 2).

189 5.1. Across-slope channels

190 Across-slope channels are perpendicular to the regional bathymetric slopes and chiefly located
191 north and south of the GH (Figures 1b and 2c). As an example, a large across-slope channel (D-D' in
192 Figures 2c and 2d), north of the GH (at $\sim 16^\circ\text{N}$), is shown as a ~ 38 km long feature with a gentle
193 thalweg dipping towards the NW (Figure 2c). As the most significant mature channel in the study
194 area, channel D-D' has the smoothest thalweg, the largest average channel width and depth, which
195 are 2.6 km and 240 m, respectively (Figures 2c and 2d). Channel D-D' is connected to the alongslope
196 channel F-F' at its southern end (Figure 2c).

197 Multiple immature channels and across-slope pockmark trains are connected to channel D-D'
198 (Figure 2c). In the southwestern part of channel D-D', immature channel E-E' has a rough thalweg
199 and is connected to channel D-D' at both its ends (Figures 2c and 2d). Channel E-E' is significantly
200 shorter (~ 20 km) than channel D-D', and it is also narrower and shallower in its width (1.1 km in
201 average) and depth (94 m in average), respectively.

202 South of the GH, where the slope gradient is $\sim 0.5^\circ$, several across-slope channels follow a SE
203 orientation (Figures 1b and 2a). Channels are roughly parallel to each other and 30 to 50 km long
204 (Figure 1b). They have rugged thalwegs and discontinuous morphologies (Figure 1b). These across-
205 slope channels have bankfull widths from 1 to 1.5 km and depths between 50 and 200 m (Figure 2c).
206 Importantly, the across-slope channel G-G' is in a zone with abundant isolated pockmarks and
207 pockmark trains (Figures 1b and 2c). Southwest of channel G-G', the across-slope channels occur on
208 the slope and remain ~ 15 km distant from the GH (Figure 1b). To the north of channel G-G', two
209 across-slope channels of ~ 14 km and ~ 18 km long reveal a relatively flat thalweg and connect to the
210 south end of the channel F-F' (Figure 2c). They are 1.5 km wide on average, and have a depth of 50-
211 150 m.

212 5.2. Alongslope channels

213 Alongslope channels are mainly observed along the south and west slopes of the ZCP and to the
214 east of the GH (Figures 2b and 2c). To the east of the GH, an alongslope channel (F-F') is identified
215 as a ~ 20 km long feature running parallel to the 800 m bathymetric contour (Figures 2a and 2c).
216 Channel F-F' has an average width of 2.6 km and its depth ranges from 150 to 180 m (Table S1).
217 Channel F-F' has a smooth thalweg and two significant topographic highs (~ 50 m high) at both its
218 ends (Figure 2d). These two highs occur at the confluences of channel F-F' with across-slope channels
219 to the north and south (Figure 2c). A small channel with a sharp bend (~ 1.5 km wide, ~ 9 km long and
220 with an average depth of 120 m), and trains of elongated pockmarks (~ 1.3 km wide and ~ 90 m deep),
221 join channel F-F' in its eastern part (Figures 1b and 2c).

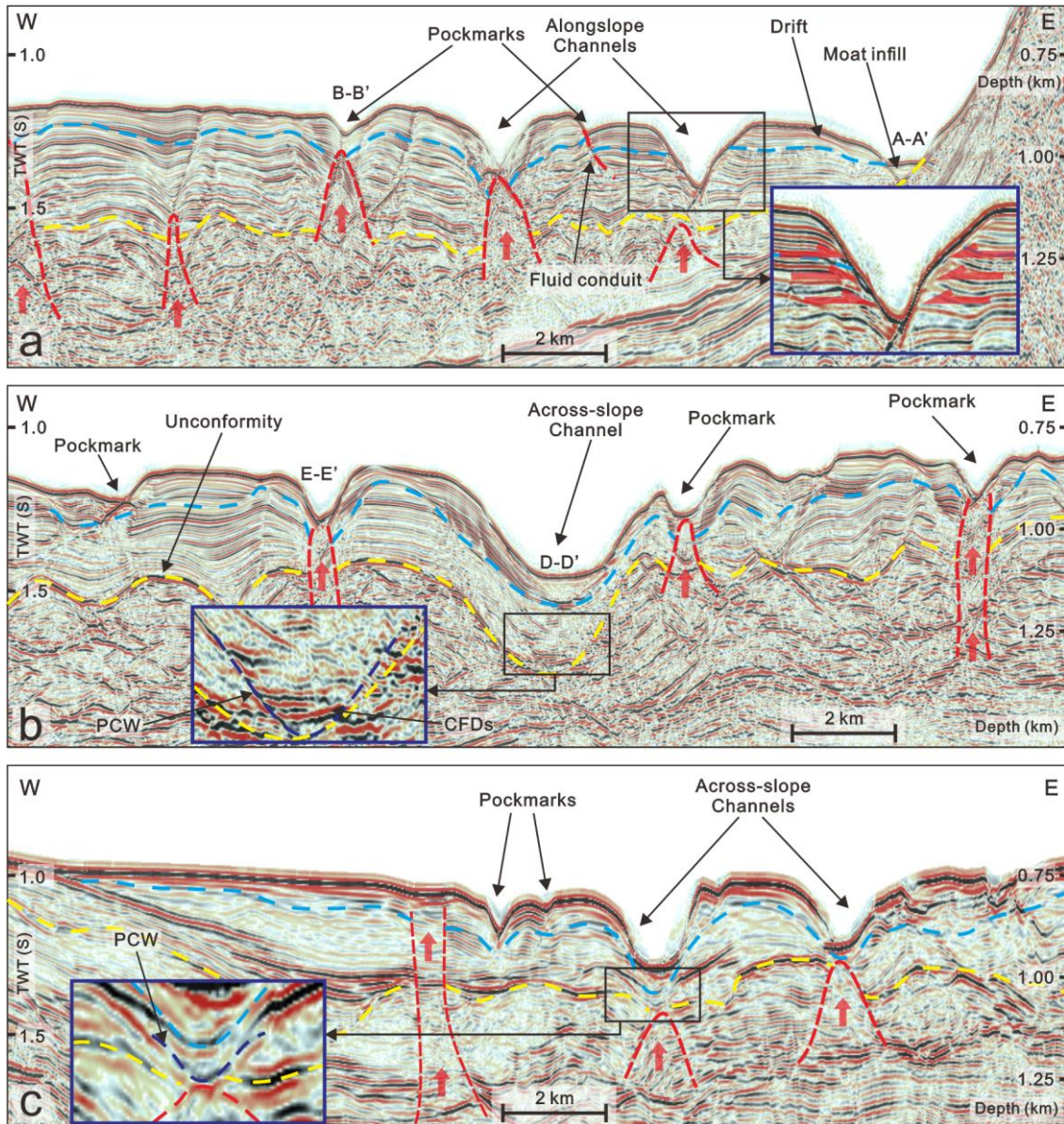
222 Alongslope channels are the most significant features around the ZCP, being parallel to the
223 platform slopes at a water depth between 1000 and 1200 m (Figures 1b and 2b). Here, the length of
224 alongslope channels ranges from 10 to 25 km, with their width varying between 1 and 2.5 km. Their
225 depth ranges between 50 and 200 m. The channel closest to the ZCP (A-A') are the shallowest, with
226 average channel depths of 73 m (Figure 1b and Table S1). These channels present elevations within

227 their thalwegs that are more than 150 m high, with slope gradients of 0.5°-0.9° (Figure 2d).
228 Furthermore, the channels closer to the ZCP, such as A-A', have smoother thalwegs and more
229 continuous plan-view morphologies when compared to more distant channels, i.e. B-B' and C-C'
230 (Figures 2b and 2d). Several elongated pockmarks and alongslope pockmark trains occur along or
231 parallel to these channels (Figure 2b).

232 5.3. Seismic architecture of channels and pockmarks

233 Seismic reflections are generally continuous and parallel between modern across-slope channels
234 (e.g. D-D') and horizon T20 (Figures 3b and 3c). In contrast, seismic reflections beneath the modern
235 alongslope channels (e.g. the channel next to A-A') are significantly truncated (Figure 3a). Chaotic
236 strata with low amplitude are rarely identified in the channel-fill deposits of modern channel (Figure
237 3). Channel D-D' is remarkably wider, and with a greater depth, when compared to the other channels
238 imaged in seismic profile (Figures 3 and S4). The inception of some channels, such as D-D', is
239 recognized between horizons T20 and T30 (Figure 3), with a limited number of channels initiated
240 below horizon T30 (Figures S4 and S6). Channel A-A' is a moat at the foot of the ZCP associated
241 with a contourite drift, it shows a typical mounded shape with internal reflections dipping towards
242 the bottom of channel A-A' (Figure 3a).

243 There are significant differences among the seismic cross-sections of across-slope and
244 alongslope channels. Alongslope channels, such as the channel next to channel A-A', show distinctive
245 truncations at their banks (Figure 3a). In contrast, across-slope channels, such as channel D-D' are
246 usually located above paleo-channels with chaotic and high amplitude seismic reflections on their
247 bases (Figs. 3b and S4). Seismic reflections on the banks of across-slope channels generally dip
248 towards the channel thalweg (Figures 2b, 2c and S4). Fluid escape features are identified as convex
249 or chaotic seismic reflections crossing particular seismic reflections (Figure 3). These fluid escape
250 features are sourced from strata older than horizon T30, and truncate the seismic reflections above
251 this same horizon (Figure 3). Most of them are connected to channels and pockmarks on the modern
252 seafloor (Figures 3, S4, S5 and S6). Some paleo-pockmarks were buried after horizon T30, while
253 some pockmarks at the modern seafloor show oblique migration since their inception (Figure 1d).



254

255 **Figure 3.** Seismic profiles (a-c) across submarine channels and seafloor pockmarks. Zoomed-in insets
256 highlight the detailed geometry of past and present-day channels. Blue and yellow dashed lines mark
257 the base of Quaternary (T20) and Pliocene (T30) strata, respectively. Fluid escape features are marked
258 in the figure by red dashed lines and red vertical arrows. Red horizontal arrows in a) mark the presence
259 of erosional truncations on the banks of alongslope channels. PCW: Paleo-channel Wall; CFDs:
260 Channel-fill Deposits. The location of the seismic profiles is shown in Figures 2b and 2c.
261

262 6. Discussion

263 6.1. Genesis of channels and their relationship to pockmark trains

264 The studied channels show variable orientations. Alongslope channels such as A-A' and F-F'
265 run parallel to the slope contours, whereas across-slope channels (D-D' and G-G') developed
266 perpendicularly to the slope topography (Figure 2). Previous studies interpreted the channels in the
267 study area as moats and furrows formed by contour currents (Yin et al., 2021). However, some of the
268 furrows and channels described in Yin et al. (2021) are perpendicular to the slope contours and, thus,

269 unlikely to be associated with contour currents flowing alongslope. Therefore, other factors probably
270 control their origin in the study area. Other oceanographic processes such as internal waves (e.g.
271 internal tides) can flow transversely to the slope, forming intense near-seafloor currents and
272 resuspending sediments, especially inside canyon (Puig et al., 2013; 2014; Aslam et al., 2018). In the
273 northern South China Sea, internal tides have been considered as a process responsible for downslope-
274 migrating sand dunes (Ma et al., 2016). Although internal tides could, in part, contribute to the erosion
275 of the interpreted channels, they are probably not the main factor controlling their origin in our study
276 area, and they may be related to gravity processes.

277 Interactions between gravity-driven processes and fluid escape in pockmarks can reshape the
278 latter to form comet-shaped pockmarks oriented perpendicularly to the slope (Chen et al., 2019), and
279 to form across-slope channels (Gay et al., 2006; Pilcher and Argent, 2007; Nakajima et al., 2014).
280 Several pockmark trains are perpendicular to the slope gradient north and south of the GH, effectively
281 comprising circular, comet-shaped and elongated pockmarks (Figure 1b). On the slopes surrounding
282 the GH, active gas seepage brings deep, unlithified sediment to the seafloor through the pockmarks,
283 while the GH comprises an active carbonate factory from where sediments are derived, contributing
284 to the occurrence of gravity flows and slumps (Gay et al., 2006; Nakajima et al., 2014; Lu et al., 2017;
285 Yang et al., 2021). Under the erosion of gravity currents on their adjacent slopes, circular pockmarks
286 were reshaped to form elongated and comet-shaped pockmarks. Furthermore, pockmarks are not only
287 scattered around the investigated channels, but also occur inside the channels themselves; hence,
288 irregular depressions in channel thalwegs are the relics of reshaped pockmarks (e.g. G-G' and E-E'
289 in Figure 2). Pre-existing pockmark trains affected by gravity currents probably contributed to the
290 formation of across-slope channels on the slopes surrounding the GH. In the study area, the paleo-
291 channels below modern across-slope channels commonly contain channel-fill deposits with chaotic
292 and high amplitude seismic reflections onlapping the bases of paleo-channels (Figs. 3b and S4). These
293 are typical seismic facies indicating the presence of gravity deposits (Figures. 3b and S4) (Wu et al.,
294 2018).

295 Contrasting with across-slope channels, there are alongslope channels such as F-F', A-A' and
296 C-C' that run parallel to the bathymetric contours (Figures 2b and 2c). They are likely formed by
297 alongslope currents. Alongslope channels identified near the foot of the GH and ZCP (e.g. F-F' and
298 A-A'; Figure 2b) are contourite moats and furrows associated with an isolated mounded drift
299 recognized by Yin et al. (2021) (Figure 3a). They are thus related to the contour currents flowing
300 along the GH and ZCP, which were strong enough to erode the seabed and generate erosional
301 truncations on the banks of alongslope channels (Figures 2a, S4 and S6). Although average bottom
302 currents are relatively weak in the western South China Sea, below 20 cm/s, they can be very variable
303 and reach a maximum velocity close to 80 cm/s (Figure S9; Yang et al., 2019). These periods of
304 intense circulation could be responsible for the observed seafloor erosion (Stow et al., 2013).

305 In addition, Andresen et al. (2008) and Kilhams et al. (2011) have suggested that bottom currents
306 can induce the erosion of pockmarks, reshaping and coalescing them along the direction of bottom
307 currents. When this process is maintained for a relatively long time, it results in the formation of
308 alongslope channels, similarly to what is observed in the southwest and southeast flanks of the ZCP
309 (Figures 1b and 2). Bottom current erosion in its broader sense is enhanced on their downstream side
310 of pockmarks to form asymmetric and elongated features (Figure 2b; Masoumi et al., 2014). The
311 elongated pockmarks are furtherly eroded and coalesce to form channels. In fact, relics of elongated
312 pockmarks are found as asymmetric depressions in some of the channel thalwegs, e.g. in channel C-
313 C' (Figure 2d).

314 6.2. Evolution of submarine channels in the western South China Sea

315 Micalef et al. (2014) first tested the concept of space-for-time substitution when reconstructing
316 the evolution of submarine canyons and channel systems on continental margins. They suggested that,
317 when the established model matches well with the morphological patterns interpreted on geophysical
318 data, time can be substituted by space to reconstruct the evolution of canyons and channels. To
319 illustrate channel development in the study area, we propose a space-for-time substitution model
320 comprising three stages: a) a channel-inception stage, in which trains of pockmarks provide favorable
321 pathways for eroding gravity flows and bottom currents, b) an immature stage, during which discrete
322 pockmarks are elongated and coalesce to form immature channels with a rugged thalweg and a
323 discontinuous morphology in plan-view, once again under the erosion of gravity flows or bottom
324 currents, c) a mature stage, in which bottom currents and gravity flows are funneled through the
325 channels to smooth their floor and banks (Figure 4). Therefore, under the erosion of gravity processes
326 and bottom currents, pockmark trains gradually form immature channels to finally evolve into a
327 complex system of across-slope and alongslope channels (Figure 4).

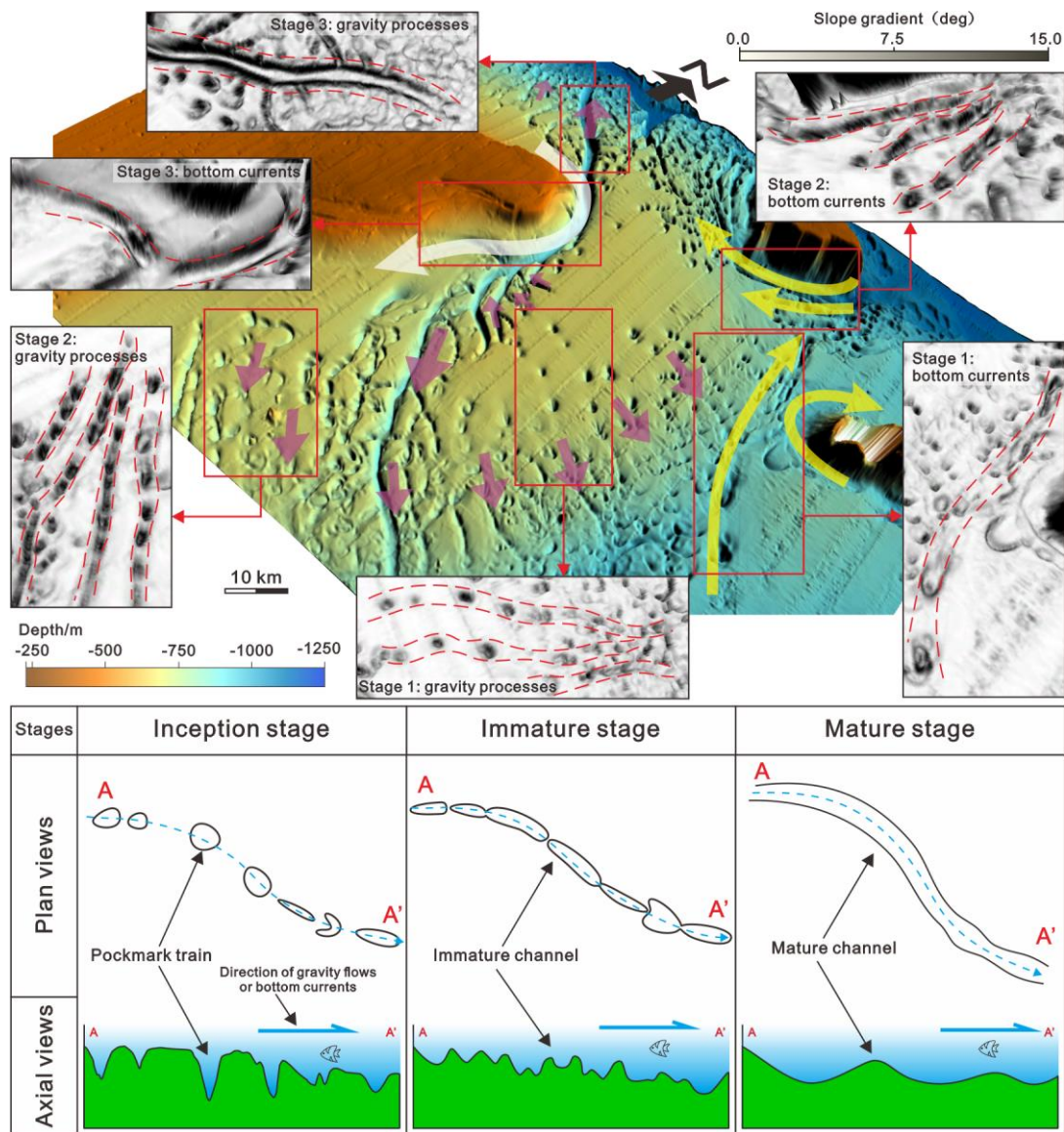
328 In the study area, Lu et al. (2017) proposed that the accumulation and dissociation of gas hydrates
329 significantly contributed to the formation of pockmarks. In parallel, Gao et al. (2019) have suggested
330 that pockmarks were formed by hydrothermal fluid flow induced by intensified hydrothermal activity
331 occurring since the Pliocene. The oldest paleo-channel below channel D-D' occurs between horizons
332 T20 and T30, suggesting the Pliocene as the time of its inception (Figures 1d and 3). Channel D-D'
333 is one of the most mature in the study area and its stratigraphic position correlates with a period of
334 enhanced hydrothermal activity in the Pliocene as identified in Gao et al. (2019). However, there are
335 differences in the timing of inception of other channels, even when considering different reaches of
336 the same channel. Some alongslope channels such as A-A' have eroded horizon T20, indicating they
337 are formed after the Pliocene (Figures 3a and S2). Other alongslope channels were identified under
338 horizon T30, on the southeastern flank of ZCP, suggesting an earlier inception (Figure S6). According
339 to the seismic data, the earliest time for channel inception in the study area can be traced to the Late
340 Miocene.

341 Seismic reflections on the banks of channel D-D', above horizon T20, are continuous and
342 parallel, but seismic reflections between horizons T20 and T30 are truncated by paleo-channels or
343 horizon T20, suggesting that erosive processes dominated during channel inception, with the resulting
344 channels becoming filled in their mature stages (Figure 3b). Widespread immature channels such as
345 E-E', and pockmark trains such as B-B', formed around mature channels also show that the
346 investigated system of channels is still evolving (Figure 2). Abundant truncations on the banks of
347 immature channels suggest that erosive processes still dominate their development (Figure 3). This
348 means that present-day immature channels can still evolve into mature features if gravity processes
349 and bottom currents keep eroding the seafloor pockmarks mapped in this work (Figure 4).

350 Channel evolution was significantly influenced by seafloor topography, which predominantly
351 controlled the dynamics of ocean currents. Changes in slope gradient can not only determine the
352 formation of channels, but also control the transition between erosional and aggradational processes
353 in them (Micalef and Mountjoy, 2011). Slope gradients differ in the north, south and east of the GH;
354 hence the steepest slope ($\sim 0.8^\circ$) north of the GH led to the formation of channel D-D', which is the
355 widest, more deeply incised of all channels. Mature and immature channels also formed on the slope
356 to the south of the GH, which records a moderate gradient of $\sim 0.5^\circ$ (Figures 2 and 4). The slope to
357 the east of the GH does not present any across-slope channels, probably because it is relatively gentle
358 ($< 0.3^\circ$) and, therefore, relatively stable and less likely to be affected by gravity processes (Figures 2
359 and 4). In addition, it is known that bathymetric obstacles influence the dynamics of bottom currents
360 and control the formation of alongslope channels (Hernández-Molina et al., 2006; Yin et al., 2021).
361 Thus, alongslope channels were commonly formed around the GH and ZCP (Figures 2).

362 Mulder et al. (2018) demonstrated that sediment supplied by channels (or canyons) onto deep-
 363 water depocenters can originate from topographic highs instead of a point source. One gully located
 364 on the eastern slope of the GH is connected to channel F-F' in a zone with a topographic high in the
 365 thalweg (Figure 2c). This zone may also contain gravity deposits transported from the platform but,
 366 unfortunately, no seismic or sediment core data were available to confirm such an assumption.
 367 Furthermore, Wu et al. (2016) revealed a similar Early Pliocene paleo-topography to the modern
 368 seafloor topography, and considered it to have an important morphological control on the
 369 development of channel systems.

370 Compared to other well-studied channels in the South China Sea (Chen et al., 2020), the channel
 371 system investigated in this work is characterized by its complicated morphology and the effect of
 372 multiple mechanisms in its development. Hence, the recognition of a system of across-slope and
 373 alongslope channels, initiated from pockmarks, and influenced by seafloor topography, has
 374 significant implications to the current understanding of how submarine channels are initiated on
 375 continental margins across the world.



376

377 **Figure 4.** Schematic diagrams, combined with a three-dimensional morphological map of the study
 378 area, summarizing the time-step evolution of channels around the interpreted pockmark field. Stage

379 1: channel inception is controlled by a pockmark train; Stage 2: under the effect of gravity processes
380 and bottom currents, discrete pockmarks are eroded and coalesce to form an immature channel; Stage
381 3: gravity processes and bottom currents continue to erode the immature channel, which subsequently
382 evolves into a mature channel presenting a smooth, continuous thalweg. The purple arrows indicate
383 the direction of gravity processes. The white and yellow arrows indicate the pathways of bottom
384 currents at water depths of ~800 m and ~1000 m, respectively.
385

386 7. Conclusions

387 High-resolution multibeam bathymetry and two-dimensional seismic data enabled us to
388 investigate the morphology of a complex system of channels in the western South China Sea, plus its
389 genesis and evolution. The main conclusions of this study are as follows:

390 (1) The studied channel system comprises a large number of across-slope and alongslope
391 channels found within a giant pockmark field, which covers an area of more than 9,000 km² at a water
392 depth of 700-1200 m.

393 (2) The channels analyzed in this study are formed by the incision of gravity processes and
394 bottom currents on seafloor pockmarks, particularly on those arranged as pockmark trains.

395 (3) Based on the space-for-time substitution concept, the evolution of the channels can be
396 summarized in three stages: Stage 1, in which the inception of the studied channels coincided with
397 the erosion of pockmark trains; Stage 2, in which pockmark trains were eroded by gravity flows and
398 bottom currents to form immature channels; Stage 3, during which immature channels evolved into
399 mature channels, with a flatter channel floor, under the effect of continuous erosion.

400 (4) The studied channel system was firstly initiated in the Late Miocene, and is still developing
401 at present. Discrete channels in this system were formed at different times, and their evolution has
402 been significantly controlled by an ever-evolving seafloor topography.
403

404 Acknowledgments

405 This work was financially supported by Key Special Project for Introduced Talents Team of
406 Southern Marine Science and Engineering Guangdong Laboratory (Guangzhou) (GML2019ZD0104),
407 Guangdong Basic and Applied Basic Research Foundation (2020B1515020016) and National
408 Scientific Foundation of China (41876054). Dr. Wei Li is funded by CAS Pioneer Hundred Talents
409 Program (Y8SL011001). We thank China National Petroleum Corporation (CNPC) for providing the
410 seismic profiles. We also thank University of Chinese Academy of Sciences (UCAS) for providing
411 the scholarship to support the research stay of Mr. Kaiqi Yu at the University of Bremen. We thank
412 Chief Editor Prof. Dr. Harihar Rajaram and the reviewers Dr. Michele Rebesco, Dr. Walter Barnhardt
413 and an anonymous reviewer for their constructive comments that helped us improve our manuscript.
414

415 Data Availability Statement

416 The seismic and bathymetric data supporting this research are owned by the China National
417 Petroleum Corporation (CNPC) and Guangzhou Marine Geological Survey (GMGS), respectively,
418 with commercial restrictions, and are not accessible to the public or research community. The seismic
419 profiles used in this study can be accessed via: <https://doi.org/10.5281/zenodo.5756961>. The
420 bathymetric data for this research are sourced from Lu et al. (2018) at <https://doi.org/10.1190/INT-2017-0222.1>.
421

422

423 **References**

- 424 Allen, P. A. (2017), Sediment routing systems: The fate of sediment from source to sink, *Cambridge*
425 *University Press*, pp.18-19.
- 426 Andresen, K. J., Huuse, M., & Clausen, O. R. (2008), Morphology and distribution of Oligocene and
427 Miocene pockmarks in the Danish North Sea - implications for bottom current activity and fluid
428 migration. *Basin Research*, **20**(3), 445-466. doi: 10.1111/j.1365-2117.2008.00362.x
- 429 Aslam, T., Hall, R. A., & Dye, S. R. (2018), Internal tides in a dendritic submarine canyon. *Progress*
430 *in Oceanography*, **169**, 20-32. doi: <https://doi.org/10.1016/j.pocean.2017.10.005>
- 431 Astakhov, A. S. (2004a), Grain size composition of bottom sediments from East Asian marginal seas,
432 core Ast-87063, edited, PANGAEA.
- 433 Astakhov, A. S. (2004b), Grain size composition of bottom sediments from East Asian marginal seas,
434 core Ast-87061, edited, PANGAEA.
- 435 Chen, H., Xie, X., Mao, K., He, Y., Su, M., & Zhang, W. (2020), Depositional Characteristics and
436 Formation Mechanisms of Deep-Water Canyon Systems along the Northern South China Sea Margin.
437 *Journal of Earth Science*, **31**(4), 808-819. doi: <https://doi.org/10.1007/s12583-020-1284-z>
- 438 Chen, TT., Paull, C. K., Liu, CS., Klaucke, I., Hsu, HH., Su, CC., Gwiazda, R., & Caress, D. W.
439 (2019), Discovery of numerous pingos and comet-shaped depressions offshore southwestern Taiwan.
440 *Geo-Marine Letters*, **40**(4), 407-421. doi: <https://doi.org/10.1007/s00367-019-00577-z>
- 441 Dandapath, S., Chakraborty, B., Karisiddaiah, S. M., Menezes, A., Ranade, G., Fernandes, W., ... &
442 Raju, K. P. (2010), Morphology of pockmarks along the western continental margin of India:
443 Employing multibeam bathymetry and backscatter data. *Marine and Petroleum Geology*, **27**(10),
444 2107-2117. doi: 10.1016/j.marpetgeo.2010.09.005
- 445 de Leeuw, J., Eggenhuisen, J. T., & Cartigny, M. J. (2016), Morphodynamics of submarine channel
446 inception revealed by new experimental approach. *Nature communications*, **7**(1), 1-7. doi:
447 10.1038/ncomms10886
- 448 Fildani, A., Hubbard, S. M., Covault, J. A., Maier, K. L., Romans, B. W., Traer, M., & Rowland, J.
449 C. (2013), Erosion at inception of deep-sea channels. *Marine and Petroleum Geology*, **41**, 48-61. doi:
450 10.1016/j.marpetgeo.2012.03.006
- 451 Gao, J., Bangs, N., Wu, S., Cai, G., Han, S., Ma, B., ... & Wang, D. (2019), Post-seafloor spreading
452 magmatism and associated magmatic hydrothermal systems in the Xisha uplift region, northwestern
453 South China Sea. *Basin Research*, **31**(4), 688-708. doi: 10.1111/bre.12338
- 454 García, M., Hernández-Molina, F. J., Llave, E., Stow, D. A. V., León, R., Fernández-Puga, M. C., ...
455 & Somoza, L. (2009), Contourite erosive features caused by the Mediterranean Outflow Water in the
456 Gulf of Cadiz: Quaternary tectonic and oceanographic implications. *Marine Geology*, **257**(1-4), 24-
457 40. doi: 10.1016/j.margeo.2008.10.009
- 458 Gay, A., Lopez, M., Cochonat, P., Séranne, M., Levaché, D., & Sermondadaz, G. (2006), Isolated
459 seafloor pockmarks linked to BSRs, fluid chimneys, polygonal faults and stacked Oligocene–
460 Miocene turbiditic palaeochannels in the Lower Congo Basin. *Marine Geology*, **226**(1-2), 25-40. doi:
461 10.1016/j.margeo.2005.09.018

- 462 Gay, A., Lopez, M., Berndt, C., & Seranne, M. (2007), Geological controls on focused fluid flow
463 associated with seafloor seeps in the Lower Congo Basin. *Marine Geology*, **244**(1-4), 68-92. doi:
464 10.1016/j.margeo.2007.06.003
- 465 Hansen, L., Janocko, M., Kane, I., & Kneller, B. (2017), Submarine channel evolution, terrace
466 development, and preservation of intra-channel thin-bedded turbidites: Mahin and Avon channels,
467 offshore Nigeria. *Marine Geology*, **383**, 146-167. doi: 10.1016/j.margeo.2016.11.011
- 468 Hernández-Molina, J., Llave, E., Somoza, L., Fernández-Puga, M. C., Maestro, A., León, R., ... &
469 Gardner, J. (2003), Looking for clues to paleoceanographic imprints: a diagnosis of the Gulf of Cadiz
470 contourite depositional systems. *Geology*, **31**(1), 19-22. [https://doi.org/10.1130/0091-](https://doi.org/10.1130/0091-7613(2003)031<0019:LFCTPI>2.0.CO;2)
471 [7613\(2003\)031<0019:LFCTPI>2.0.CO;2](https://doi.org/10.1130/0091-7613(2003)031<0019:LFCTPI>2.0.CO;2)
- 472 Hernández-Molina, F. J., Larter, R. D., Rebesco, M., & Maldonado, A. (2006), Miocene reversal of
473 bottom water flow along the Pacific Margin of the Antarctic Peninsula: stratigraphic evidence from
474 a contourite sedimentary tail. *Marine Geology*, **228**(1-4), 93-116. doi: 0.1016/j.margeo.2005.12.010
- 475 Hillman, J. I., Klauke, I., Pecher, I. A., Gorman, A. R., Schneider von Deimling, J., & Bialas, J.
476 (2018), The influence of submarine currents associated with the Subtropical Front upon seafloor
477 depression morphologies on the eastern passive margin of South Island, New Zealand. *New Zealand*
478 *Journal of Geology and Geophysics*, **61**(1), 112-125. doi: 10.1080/00288306.2018.1434801
- 479 Hovland, M., Gardner, J. V., & Judd, A. G. (2002), The significance of pockmarks to understanding
480 fluid flow processes and geohazards. *Geofluids*, **2**(2), 127-136. doi: 10.1046/j.1468-8123.2002.
481 00028.x
- 482 Kilhams, B., McArthur, A., Huuse, M., Ita, E., & Hartley, A. (2011), Enigmatic large-scale furrows
483 of Miocene to Pliocene age from the central North Sea: current-scoured pockmarks. *Geo-Marine*
484 *Letters*, **31**(5), 437-449. doi: 10.1007/s00367-011-0235-1
- 485 Lemay, M., Grimaud, J. L., Cojan, I., Rivoirard, J., & Ors, F. (2020), Geomorphic variability of
486 submarine channelized systems along continental margins: Comparison with fluvial meandering
487 channels. *Marine and Petroleum Geology*, **115**. doi: 10.1016/j.marpetgeo.2020.104295
- 488 León, R., Somoza, L., Medialdea, T., Hernández-Molina, F. J., Vázquez, J. T., Díaz-del-Río, V., &
489 González, F. J. (2010), Pockmarks, collapses and blind valleys in the Gulf of Cádiz. *Geo-Marine*
490 *Letters*, **30**(3-4), 231-247. doi: 10.1007/s00367-009-0169-z
- 491 Li, C. F., Xu, X., Lin, J., Sun, Z., Zhu, J., Yao, Y., ... & Zhang, G. L. (2014), Ages and magnetic
492 structures of the South China Sea constrained by deep tow magnetic surveys and IODP Expedition
493 349. *Geochemistry, Geophysics, Geosystems*, **15**(12), 4958-4983. doi:
494 <https://doi.org/10.1002/2014GC005567>
- 495 Li, W., Alves, T. M., Wu, S., Völker, D., Zhao, F., Mi, L., & Kopf, A. (2015), Recurrent slope failure
496 and submarine channel incision as key factors controlling reservoir potential in the South China Sea
497 (Qiongdongnan Basin, South Hainan Island). *Marine and Petroleum Geology*, **64**, 17-30.
498 doi:10.1002/2014GC005567.
- 499 Liu, Q., Kaneko, A., & Jilan, S. (2008), Recent progress in studies of the South China Sea circulation.
500 *Journal of Oceanography*, **64**(5), 753-762. doi: 10.1007/s10872-008-0063-8
- 501 Lu, Y., Li, W., Wu, S., Cronin, B. T., Lyu, F., Wang, B., ... & Ma, B. (2018), Morphology,
502 architecture, and evolutionary processes of the Zhongjian Canyon between two carbonate platforms,
503 South China Sea. *Interpretation*, **6**(4), SO1-SO15. doi: <https://doi.org/10.1190/INT-2017-0222.1>

- 504 Lu, Y., Luan, X., Lyu, F., Wang, B., Yang, Z., Yang, T., & Yao, G. (2017), Seismic evidence and
505 formation mechanism of gas hydrates in the Zhongjiannan Basin, Western margin of the South China
506 Sea. *Marine and Petroleum Geology*, **84**, 274-288. doi: 10.1016/j.marpetgeo.2017.04.005
- 507 Ma, X., Yan, J., Hou, Y., Lin, F., & Zheng, X. (2016), Footprints of obliquely incident internal solitary
508 waves and internal tides near the shelf break in the northern South China Sea. *Journal of Geophysical*
509 *Research: Oceans*, **121**(12), 8706-8719. doi: 10.1002/2016JC012009
- 510 Masoumi, S., Reuning, L., Back, S., Sandrin, A., & Kukla, P. A. (2014), Buried pockmarks on the
511 Top Chalk surface of the Danish North Sea and their potential significance for interpreting
512 palaeocirculation patterns. *International Journal of Earth Sciences*, **103**(2), 563-578. doi:
513 10.1007/s00531-013-0977-2
- 514 Micallef, A., & Mountjoy, J. J. (2011), A topographic signature of a hydrodynamic origin for
515 submarine gullies. *Geology*, **39**(2), 115-118. <https://doi.org/10.1130/G31475.1>
- 516 Micallef, A., Ribó, M., Canals, M., Puig, P., Lastras, G., & Tubau, X. (2014), Space-for-time
517 substitution and the evolution of a submarine canyon–channel system in a passive progradational
518 margin. *Geomorphology*, **221**, 34-50. doi: 10.1016/j.geomorph.2014.06.008
- 519 Miramontes, E., Jouet, G., Thereau, E., Bruno, M., Penven, P., Guerin, C., ... & Cattaneo, A. (2020),
520 The impact of internal waves on upper continental slopes: insights from the Mozambican margin (SW
521 Indian Ocean). *Earth Surface Processes and Landforms*, **45**(6), 1469-1482. doi: 10.1002/esp.4818
- 522 Miramontes, E., P. Garreau, M. Caillaud, G. Jouet, R. Pellen, F. J. Hernández-Molina, M. A. Clare,
523 & A. Cattaneo (2019), Contourite distribution and bottom currents in the NW Mediterranean Sea:
524 Coupling seafloor geomorphology and hydrodynamic modelling. *Geomorphology*, **333**, 43-60. doi:
525 10.1016/j.geomorph.2019.02.030
- 526 Miramontes, E., Thiéblemont, A., Babonneau, N., Penven, P., Raison, F., Droz, L., ... & Jouet, G.
527 (2021), Contourite and mixed turbidite-contourite systems in the Mozambique Channel (SW Indian
528 Ocean): Link between geometry, sediment characteristics and modelled bottom currents. *Marine*
529 *Geology*, **437**, 106502. doi: <https://doi.org/10.1016/j.margeo.2021.106502>
- 530 Mulder, T., Gillet, H., Hanquiez, V., Ducassou, E., Fauquembergue, K., Principaud, M., ... & Seibert,
531 C. (2018). Carbonate slope morphology revealing a giant submarine canyon (Little Bahama Bank,
532 Bahamas). *Geology*, **46**(1), 31-34. doi: <https://doi.org/10.1130/G39527.1>
- 533 Nakajima, T., Kakuwa, Y., Yasudomi, Y., Itaki, T., Motoyama, I., Tomiyama, T., ... & Matsumoto,
534 R. (2014), Formation of pockmarks and submarine canyons associated with dissociation of gas
535 hydrates on the Joetsu Knoll, eastern margin of the Sea of Japan. *Journal of Asian Earth Sciences*,
536 **90**, 228-242. doi: <https://doi.org/10.1016/j.jseaes.2013.10.011>
- 537 Pilcher, R., & Argent, J. (2007), Mega-pockmarks and linear pockmark trains on the West African
538 continental margin. *Marine Geology*, **244**(1-4), 15-32. doi: 10.1016/j.margeo.2007.05.002
- 539 Puig, P., Palanques, A., & Martín, J. (2014), Contemporary sediment-transport processes in
540 submarine canyons. *Annual Review of Marine Science*, **6**, 53-77. doi: 10.1146/annurev-marine-
541 010213-135037
- 542 Puig, P., Greenan, B. J., Li, M. Z., Prescott, R. H., & Piper, D. J. (2013), Sediment transport processes
543 at the head of Halibut Canyon, eastern Canada margin: An interplay between internal tides and dense
544 shelf-water cascading. *Marine Geology*, **341**, 14-28. doi:10.1016/j.margeo.2013.05.004
- 545 Quan, Q., & Xue, H. (2018), Layered model and insights into the vertical coupling of the South China
546 Sea circulation in the upper and middle layers. *Ocean Modelling*, **129**, 75-92. doi:
547 10.1016/j.ocemod.2018.06.006

- 548 Rebesco, M., Hernández-Molina, F. J., Van Rooij, D., & Wåhlin, A. (2014), Contourites and
549 associated sediments controlled by deep-water circulation processes: State-of-the-art and future
550 considerations. *Marine Geology*, **352**, 111-154. doi: 10.1016/j.margeo.2014.03.011
- 551 Sancaktar, E., & R. Gomatam (2001), A study on the effects of surface roughness on the strength of
552 single lap joints, *Journal of Adhesion Science and Technology*, **15**(1), 97-117. doi:
553 10.1163/156856101743346
- 554 Stow, D. A. V., Hernández-Molina, F. J., Llave, E., Bruno, M., García, M., del Rio, V. D., ... &
555 Brackenridge, R. E. (2013), The Cadiz Contourite Channel: Sandy contourites, bedforms and
556 dynamic current interaction. *Marine Geology*, **343**, 99-114. doi: 10.1016/j.margeo.2013.06.013
- 557 Wu, S., Zhang, X., Yang, Z., Wu, T., Gao, J., & Wang, D. (2016), Spatial and temporal evolution of
558 Cenozoic carbonate platforms on the continental margins of the South China Sea: Response to
559 opening of the ocean basin. *Interpretation*, **4**(3), SP1-SP19. doi: <https://doi.org/10.1190/INT-2015-0162.1>
- 561 Wu, W., Li, Q., Yu, J., Lin, C., Li, D., & Yang, T. (2018), The Central Canyon depositional patterns
562 and filling process in east of Lingshui Depression, Qiongdongnan Basin, northern South China Sea.
563 *Geological Journal*, **53**(6), 3064-3081. doi: <https://doi.org/10.1002/gj.3143>
- 564 Yang, Yuanzheng., Xu. C., Li. S., & He. Y. (2019), Ship-mounted ADCP data for ocean currents in
565 the South China Sea (2009–2012). doi: 10.11922/csdata.2019.0006.zh
- 566 Yang, Z., Li, X., Huang, L., Wang, L., Wu, S., & Zhang, X. (2021), Development of the Miocene
567 Guangle Carbonate Platform in the South China Sea: Architecture and Controlling Factors. *Acta*
568 *Geologica Sinica - English Edition*, **95**(1), 177-191. doi: 10.1111/1755-6724.14639
- 569 Yin, S., Hernández-Molina, F. J., Lin, L., Chen, J., Ding, W., & Li, J. (2021), Isolation of the South
570 China Sea from the North Pacific Subtropical Gyre since the latest Miocene due to formation of the
571 Luzon Strait. *Scientific Reports*, **11**(1), 1562. doi: 10.1111/1755-6724.14639
- 572 Zhou, D., Ru, K., & Chen, H. Z. (1995), Kinematics of Cenozoic extension on the South China Sea
573 continental margin and its implications for the tectonic evolution of the region. *Tectonophysics*,
574 **251**(1-4), 161-177. doi: 10.1016/0040-1951(95)00018-6
- 575 Zhu, M., Graham, S., Pang, X., & McHargue, T. (2010), Characteristics of migrating submarine
576 canyons from the middle Miocene to present: Implications for paleoceanographic circulation,
577 northern South China Sea. *Marine and Petroleum Geology*, **27**(1), 307-319. doi:
578 10.1016/j.marpetgeo.2009.05.005